INTERNATIONAL JOURNAL FOR NUMERICAL METHODS IN BIOMEDICAL ENGINEERING
Int. J. Numer. Meth. Biomed. Engng. 2011; **27**:2021–2034

Modeling a semi-flexible filament in cellular Stokes flow using regularized Stokeslets

Elizabeth L. Bouzarth[1,*,†], Anita T. Layton[1] and Yuan-Nan Young[2]

[1]*Department of Mathematics, Duke University, Box #90320, Durham, NC 27708, USA*
[2]*Department of Mathematical Sciences, University Heights, New Jersey Institute of Technology, Newark, NJ 07102, USA*

SUMMARY

Many physical and biological systems involve inextensible fibers immersed in a fluid; examples include cilia, polymer suspensions, and actin filament transport. In such systems, the dynamics of the immersed fibers may play a significant role in the observed macroscale fluid dynamics. In this study, we simulate the dynamics of an approximately inextensible semi-flexible fiber immersed in a two-dimensional cellular background flow. The system is modeled as an immersed boundary problem with the fluid dynamics described using the Stokes equations. The motion of the immersed fiber is computed by means of the method of regularized Stokeslets, which allows one to calculate fluid velocity, pressure, and stress in the Stokes fluid flow regime because of a collection of regularized point forces without computing fluid velocities on an underlying grid. Simulation results show that, for some parameter values, the fiber may buckle when approaching a stagnation point. These results provide insight into the stretch–coil transition and macroscale random walk behavior that have been reported in mathematical and experimental literature. Copyright © 2011 John Wiley & Sons, Ltd.

Received 19 October 2010; Revised 1 April 2011; Accepted 13 May 2011

KEY WORDS: Stokes flow; regularized Stokeslets; immersed filament

1. INTRODUCTION

Elastic, semi-flexible slender bodies are responsible for a great variety of biological functions, which are carried out by the hydrodynamics of these bodies immersed in viscous fluids. One example of such slender bodies is the cilium, which consists of a bundle of bio-polymers known as microtubules. The dynamics of multiple pulmonary cilia assist in transporting mucus in the lung. Another type of cilia, primary cilia, extend from the membrane of a cell or a unicellular organism. Some of these cilia are immotile and act as sensors, whereas others are capable of rhythmical motion, acting in unison with other surface structures to bring about the movement of the cell of the surrounding medium. The motion of primary cilia has been linked to the breaking of left–right asymmetry in developing embryos [1–5]. Another example is the motion of a flagellum that is driven by motor proteins. This motion is responsible for the locomotion of bacteria in its surrounding fluid [6–8].

The hydrodynamics of a single bio-polymer, such as DNA, actin filaments, or microtubules, have also been widely investigated. DNA molecules are flexible filaments, and a great deal of effort has been devoted to the folding and unfolding of DNA strands in planar shear flow or extensional flow. Actins and microtubules are semi-flexible slender filaments. When driven by molecular motors

---

[*] Correspondence to: Elizabeth L. Bouzarth, Department of Mathematics, Duke University, Box #90320, Durham, NC 27708, USA.

[†] E-mail: bouzarth@math.duke.edu

in the motility assays, microtubules have been utilized for transporting nano-cargo in microfluidic channels [9, 10]. Many bio-fluidic and nano-fluidic systems involve conversion of chemical energy to mechanical work for transport at small scales. For example, in the *in vitro* motility assays, microtubules (or actins) are driven by kinesins (or myosins), which convert the chemical energy of adenosine triphosphate hydrolysis into mechanical work [11–13]. The principal mechanism for transport of actins or microtubules in the motility assays has been utilized in emerging nanotechnology for directed transport of molecules and nanometer-sized cargo in cellular-sized synthetic devices [14–19]. Results from these studies are essential for direct molecular assembling, sorting, and sensing [20–22]. By integrating motor proteins into synthetic devices, it is possible to assemble a shuttle system where nano-scale cargo is transported between user-defined locations for specific cargo delivery. Electric fields [23] and hydrodynamic flows [24] have been utilized to direct the transport of shuttles in the assays.

Coarse-grained bead-rod and bead-spring models have been widely used for Monte-Carlo simulations of bio-polymers [25–27]. Whereas it is easy to implement the coarse-grained models for qualitative comparison with experiments, a continuum formulation (such as a slender-body formulation [28, 29]) allows analysis for elucidating the underlying physics. However, the far-field fluid flow is not accurately described by the slender-body equations; also, the slender-body equations become invalid when elastic structures are in close vicinity of each other. The immersed boundary method may be used to simulate fluid–structure interaction [30], but the computational cost required to accurately capture the elastic dynamics of slender filaments immersed in a viscous fluid may be high.

In this paper, we will utilize the method of regularized Stokeslets [31, 32] to model a semi-flexible, approximately inextensible fiber immersed in two-dimensional cellular Stokes flow. This method provides a way to calculate fluid flow properties due to the dynamic forces generated by an immersed structure without requiring an underlying fluid grid. Additionally, the method of regularized Stokeslets can be used to calculate the stress and pressure at any point in the fluid. Regularized Stokeslets have been used to model a variety of biological contexts, including cilia, bacterial flagellar bundling and swimming, arthropod filiform hairs, microorganism locomotion, and endothelial glycocalyx structures [32–37].

The remainder of this paper is organized as follows. Section 2 introduces the physical scenario of interest in this study. Section 3 explores aspects of our numerical implementation, including an introduction to the method of regularized Stokeslets and a discussion of our semi-implicit time-stepping technique. Numerical results are presented in Sections 4 and 5, which show qualitative agreement with experimental and modeling literature [29, 38] and provide new information.

2. MODEL AND PHYSICAL SETUP

We describe a mathematical model that simulates the physical experiments by Wandersman *et al.* [38], in which a slender inextensible semi-flexible fiber is immersed in a shallow fluid. The depth of the fluid is such that the flow is considered to be two dimensional. This cellular flow has a lattice of stagnation points, each consisting of a stable and an unstable manifold. The length of the fiber in the experiments is 12 mm. With that length scale, the flow is characterized by a low Reynolds number, indicating that viscous forces dominate inertial forces. Thus, we describe the fluid flow using the quasi-steady Stokes equations in two dimensions in free space, given by

$$\mu \Delta \mathbf{u} = \nabla p - \mathbf{F}, \tag{1}$$

$$\nabla \cdot \mathbf{u} = 0, \tag{2}$$

where μ is the dynamic viscosity of the fluid, $\mathbf{u}$ represents the fluid velocity, p represents pressure, and $\mathbf{F}$ is an external force exerted on the fluid, which will be discussed further in the succeeding paragraphs. In this regime, the time-varying fluid flow can be calculated at each time instant from only the current configuration (a consequence of the low Reynolds approximation that neglects inertial terms in the Navier–Stokes equations).

The fiber, assumed to have length L, is immersed in the following background flow velocity:

$$\mathbf{u}_{\mathrm{bg}}(\mathbf{x}) = u_0 \begin{bmatrix} \sin\left(\frac{\pi x}{W}\right)\cos\left(\frac{\pi y}{W}\right) \\ \\ -\cos\left(\frac{\pi x}{W}\right)\sin\left(\frac{\pi y}{W}\right) \end{bmatrix}, \tag{3}$$

where u_0 scales the maximum flow velocity and W dictates the width of a cell. Figure 1 exhibits the background flow velocity, depicted for four cells. Let $\alpha = \frac{L}{W}$ be the ratio between the fiber length and cell width. Unless otherwise noted, $\alpha = 0.4$ in this study.

To model an approximately inextensible, semi-flexible fiber, we assume the fiber is elastic so that when it is stretched or compressed, it exerts an elastic force, $\mathbf{f}_{\mathrm{e}}$, on the fluid. Also, when the fiber is bent, it exerts a bending force, $\mathbf{f}_{\mathrm{b}}$, on the fluid. Let Γ be the fiber; $s(t)$, the arc length along Γ at time t; $\mathbf{X}(s)$, the position of a point on the fiber; and ξ, the arc length of the fiber in its equilibrium position. Note that for a truly inextensible fiber, $s(t) = \xi$ for all t. However, our model fiber is allowed a small degree of extension or compression (see succeeding discussions); thus, $s(t)$ does not necessarily equal ξ. As such, the elastic force is given by

$$\mathbf{f}_{\mathrm{e}}(s) = \frac{\partial}{\partial s}\left(T(s)\hat{\boldsymbol{\tau}}(s)\right), \tag{4}$$

where T is the tension in the fiber and $\hat{\boldsymbol{\tau}}$ is the unit tangent vector to the fiber, each respectively given by

$$T(s) = T_0\left(\left|\frac{\partial \mathbf{X}}{\partial \xi}\right| - 1\right), \tag{5}$$

$$\hat{\boldsymbol{\tau}}(s) = \frac{\partial \mathbf{X}}{\partial s}. \tag{6}$$

The tension coefficient, T_0, is a material property of the fiber. To approximate an inextensible fiber, T_0 will be large. The bending force is given by

$$\mathbf{f}_{\mathrm{b}} = c_{\mathrm{b}}\mathbf{X}_{ssss}, \tag{7}$$

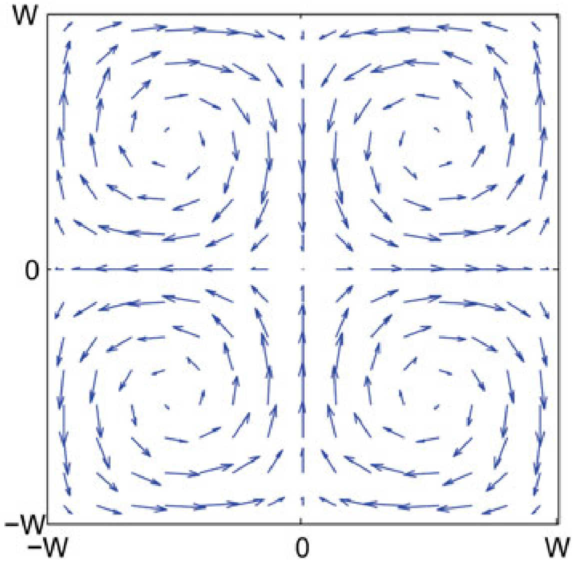

Figure 1. Two-dimensional cellular background flow given in Equation (3). Note that only four cells are represented in the figure, but an infinite number of cells are assumed in the model. The cell pattern is repeated periodically in both the x and y directions. There are no physical boundaries in this fluid, except the immersed structure.

DOI: 10.1002/cnm

with $\mathbf{X}_{ss} = 0$ and $\mathbf{X}_{sss} = 0$ enforced at the endpoints of the fiber to ensure the fiber is force free. Here, c_{b} is the bending coefficient.

The velocity at any point in the fluid can then be decomposed as follows with $\mathbf{u}_{\mathrm{bg}}$, $\mathbf{u}_{\mathrm{e}}$, and $\mathbf{u}_{\mathrm{b}}$ representing the background velocity from Equation (3), the velocity due to elastic forces, and the velocity due to bending forces, respectively,

$$\mathbf{u}(\mathbf{x}) = \mathbf{u}_{\mathrm{bg}}(\mathbf{x}) + \mathbf{u}_{\mathrm{e}}(\mathbf{x}) + \mathbf{u}_{\mathrm{b}}(\mathbf{x}). \tag{8}$$

In two dimensions, let $\mathbf{u}(\mathbf{x}) = (u_1(\mathbf{x}), u_2(\mathbf{x}))$. Incorporating the aforementioned elastic and bending forces, the ith component of the velocity at a fluid location $\mathbf{x}$ is

$$u_i(\mathbf{x}) = u_{\mathrm{bg},i}(\mathbf{x}) + \int_{\Gamma} \sum_{j=1}^{2} \tilde{S}_{ij}(\mathbf{x}, \mathbf{X}(s)) \left[f_{\mathrm{e},j}(\mathbf{X}(s)) + f_{\mathrm{b},j}(\mathbf{X}(s)) \right] \mathrm{d}s, \tag{9}$$

where $i = 1, 2$. Here, $\tilde{S}$ is the free-space Green's function, or Stokeslet,

$$\tilde{S}_{ij}(\mathbf{x}, \mathbf{X}) = \frac{1}{4\pi\mu} \left[-\delta_{ij} \ln |\mathbf{x} - \mathbf{X}| + \frac{(x_i - X_i)(x_j - X_j)}{|\mathbf{x} - \mathbf{X}|^2} \right], \tag{10}$$

which will be discussed further in Section 3.1.

3. NUMERICAL METHOD

The velocity expression in Equation (9) has a singularity when the velocity is calculated at the location of the point force, due to the Stokeslet given in Equation (10). This is undesirable numerically because quadrature error will be large when evaluating the boundary integral near the immersed fiber. As such, we will work with a modified version of the Stokeslet that results in computing the free-space Green's function due to a regularized point force. By using the method of regularized Stokeslets, we remove the singular nature from the velocity expression. The details of the method of regularized Stokeslets are summarized in Section 3.1.

3.1. Method of regularized Stokeslets

The method of regularized Stokeslets, originally developed by Cortez [31, 32], is a grid-free numerical method that calculates the fluid velocity in Stokes flow due to a collection of regularized forces. In traditional singularity theory, a Stokeslet is the free-space Green's function resulting from a singular force that is represented by a Dirac delta distribution, as shown in Equation (10) (see [39] for more information regarding Stokeslets and related singularities). In the method of regularized Stokeslets, cutoff functions are introduced in lieu of Dirac deltas to regularize Stokeslets. This regularization removes the singular nature from the velocity field; hence, the velocity and other fluid quantities of interest, such as stress and pressure, can be evaluated anywhere in the fluid, including at the location of a regularized Stokeslet. After regularizing a singular force, there exists a linear relationship between regularized Stokeslet forces and the velocity anywhere in the fluid.

The details of the method of regularized Stokeslets in two dimensions are summarized in the succeeding discussions [31]. Instead of representing a point force with a delta function, as is the case in deriving a Stokeslet, we regularize the force using a radially symmetric cutoff function, ϕ_ϵ. We assume that the cutoff function is a smooth approximation to the delta function that satisfies the following conditions:

$$\int \phi_\epsilon(\mathbf{x}) \mathrm{d}\mathbf{x} = 1, \tag{11}$$

$$\lim_{\epsilon \to 0} \phi_\epsilon(\mathbf{x}) = \delta(\mathbf{x}), \tag{12}$$

where ϵ is a spreading parameter that controls the extent of the distribution. Following [31], we use the cutoff function

$$\phi_\epsilon(r) = \frac{3\epsilon^3}{2\pi(r^2+\epsilon^2)^{5/2}}, \tag{13}$$

where $r = |\mathbf{x} - \mathbf{x_0}|$, with the regularized point force located at $\mathbf{x_0}$.

Now consider solving the Stokes equations in two dimensions with a regularized forcing term at $\mathbf{x_0}$, with $\hat{\mathbf{x}} = \mathbf{x} - \mathbf{x_0}$

$$\mu\Delta\mathbf{u}(\mathbf{x}) = \nabla p(\mathbf{x}) - \mathbf{f}\phi_\epsilon(\hat{\mathbf{x}}), \tag{14}$$

$$\nabla\cdot\mathbf{u}(\mathbf{x}) = 0. \tag{15}$$

One can represent a solution to Equations (14) and (15) in two dimensions with a regularized Stokeslet constructed from the cutoff function ϕ_ϵ [31]

$$S_{ij}^{\phi_\epsilon}(\mathbf{x},\mathbf{x_0}) = \delta_{ij}F_1(r,\epsilon) + \hat{x}_i\hat{x}_jF_2(r,\epsilon), \tag{16}$$

where $i = 1,2$ and $j = 1,2$ and

$$F_1(r,\epsilon) = -\ln\left(\sqrt{r^2+\epsilon^2}+\epsilon\right) + \epsilon\left(\sqrt{r^2+\epsilon^2}+2\epsilon\right)\left(\sqrt{r^2+\epsilon^2}+\epsilon\right)\sqrt{r^2+\epsilon^2}, \tag{17}$$

$$F_2(r,\epsilon) = \frac{\sqrt{r^2+\epsilon^2}+2\epsilon}{\left(\sqrt{r^2+\epsilon^2}+\epsilon\right)^2\sqrt{r^2+\epsilon^2}}. \tag{18}$$

Notice that in the limit as $\epsilon \to 0$, we recover the expression for the singular Stokeslet in two dimensions

$$\lim_{\epsilon\to 0} S_{ij}^{\phi_\epsilon} = -\delta_{ij}\ln r + \frac{\hat{x}_i\hat{x}_j}{r^2} = S_{ij}, \tag{19}$$

where $S_{ij} = 4\pi\mu\tilde{S}_{ij}$ from Equation (10) [31,39].

The velocity at a fluid location $\mathbf{x}$ due to a regularized point force located at $\mathbf{x_0}$ can be represented as

$$u_i^{S,\phi_\epsilon}(\mathbf{x}) = \frac{1}{4\pi\mu}\sum_{j=1}^{2} S_{ij}^{\phi_\epsilon}(\mathbf{x},\mathbf{x_0})f_j. \tag{20}$$

Additionally, one can find the pressure at a fluid location $\mathbf{x}$ due to a regularized point force at $\mathbf{x_0}$ as [31]

$$p(\mathbf{x}) = \frac{1}{2\pi}P_j^{\phi_\epsilon}f_j, \tag{21}$$

where

$$P_j^{\phi_\epsilon} = \frac{\hat{x}_j\left(r^2+2\epsilon^2+\epsilon\sqrt{r^2+\epsilon^2}\right)}{(\sqrt{r^2+\epsilon^2}+\epsilon)(r^2+\epsilon^2)^{3/2}}. \tag{22}$$

From the velocity and pressure expressions, one can also derive the stress

$$\sigma_{ij} = -p\delta_{ij} + \mu\left(\frac{\partial u_i}{\partial x_j} + \frac{\partial u_j}{\partial x_i}\right) \tag{23}$$

$$= T_{ikj}^{\phi_\epsilon}f_j, \tag{24}$$

where

$$T^{\phi_\epsilon}_{ikj} = \delta_{ik}\hat{x}_j F_3 + (\delta_{ij}\hat{x}_k + \delta_{jk}\hat{x}_i)F_4 + 4\hat{x}_i\hat{x}_j\hat{x}_k F_5, \tag{25}$$

$$F_3 = \frac{-2\epsilon^2(2(r^2+\epsilon^2)^{1/2}+\epsilon)}{(r^2+\epsilon^2)^{3/2}((r^2+\epsilon^2)^{1/2}+\epsilon)^2}, \tag{26}$$

$$F_4 = \frac{-4\epsilon^2}{(r^2+\epsilon^2)((r^2+\epsilon^2)^{1/2}+\epsilon)^2}, \tag{27}$$

$$F_5 = \frac{1}{(r^2+\epsilon^2)^{3/2}((r^2+\epsilon^2)^{1/2}\epsilon)} + \frac{\epsilon}{(r^2+\epsilon^2)((r^2+\epsilon^2)^{1/2}+\epsilon)^3}. \tag{28}$$

This stress calculation is an advantage of using the method of regularized Stokeslets to model the immersed fiber scenario of interest in this paper. The local interaction of the buckling fiber with the surrounding fluid is responsible for interesting macroscale behavior, so investigating the stress in this configuration will be beneficial.

With the aforementioned regularized Stokeslet formulation, by knowing the forces exerted on the fluid, we can compute the fluid velocity, pressure, and stress at any point in the infinite two-dimensional fluid domain. The position of the fiber $\mathbf{X}(s)$ is represented by N discrete points initially equally spaced with respect to s. Notationally, let $\mathbf{X}_k$ represent the location of the kth regularized Stokeslet on the fiber, where $k = 1, \ldots, N$. When discretizing the regularized version of Equation (9), the velocity can be expressed as

$$u_i(\mathbf{x}) = u_{\mathrm{bg},i}(\mathbf{x}) + \sum_{k=1}^{N}\sum_{j=1}^{2} q_k S^{\phi_\epsilon}_{ij}(\mathbf{x}, \mathbf{X}_k)\left[f_{\mathrm{e},j}(\mathbf{X}_k) + f_{\mathrm{b},j}(\mathbf{X}_k)\right], \tag{29}$$

where q_k is a quadrature weight. For the work discussed here, we use the trapezoid rule for integral approximations. The elastic and bending forces discussed in Section 2 can be expressed as a linear function of fiber position, $\mathbf{X}_k$. By incorporating this formulation into Equation (29), we obtain the following:

$$u_i(\mathbf{x}) = u_{\mathrm{bg},i}(\mathbf{x}) + \sum_{k=1}^{N}\sum_{j=1}^{2}\sum_{l=1}^{2} q_k S^{\phi_\epsilon}_{ij}(\mathbf{x}, \mathbf{X}_k)\left(A_{e,jl} + A_{b,jl}\right)X_{k,l}, \tag{30}$$

where A_{e} and A_{b} represent the discrete operators associated with the elastic and bending forces, respectively. For the results shown in this paper, A_{e} arises from a discretization using a second-order centered difference method, and A_{b} is associated with a second-order, non-uniform, five-point finite difference stencil. Recall, in this notation, that $\mathbf{X}$ represents all discretized fiber locations (hence, all regularized Stokeslets locations), and $\mathbf{x}$ represents all locations where we want to calculate the fluid velocity. Thus, $\mathbf{x}$ could equal just $\mathbf{X}$ or it could include fluid locations in addition to those contained in $\mathbf{X}$. The formulation in Equation (30) can be adapted to deal with both of these situations, regardless of whether the fluid velocity is desired only at locations that coincide with regularized Stokeslets or elsewhere.

3.2. *Semi-implicit time stepping*

With Equation (30) discretized in space, we can advance the fiber position as well as the fluid tracer locations in time using a time-stepping algorithm described in the succeeding paragraphs. The velocity contributions due to the fiber's position are stiff contributions to the ODE system. Specifically, the bending force is calculated with a high-order derivative, and the inextensibility condition is implemented with a collection of stiff springs. Thus, using an explicit method requires a prohibitively small time step. However, using a fully implicit time-stepping method involves solving a nonlinear system of equations, which can also be undesirable. To balance these concerns, we implement a semi-implicit treatment of the velocity decomposition in Equation (30). To condense notation, we consider Equation (30) in vector form, rather than component form

$$\mathbf{u}(\mathbf{x}) = \mathbf{u}_{\mathrm{bg}}(\mathbf{x}) + M(\mathbf{x}, \mathbf{X})\mathbf{X}, \tag{31}$$

where $\mathbf{u}(\mathbf{x})$ and $\mathbf{u}_{\mathrm{bg}}(\mathbf{x})$ denote fluid velocities at the locations $\mathbf{x}$. The matrix M is given by

$$M(\mathbf{x}, \mathbf{X}) = \sum_{k=1}^{N} q_k S^{\phi_\epsilon}(\mathbf{x}, \mathbf{X}_k)(A_{\mathrm{e}} + A_{\mathrm{b}}). \tag{32}$$

We will consider two cases: when the fluid velocity is calculated at a regularized Stokeslet location ($\mathbf{x} = \mathbf{X}$) and when the velocity is calculated away from a regularized Stokeslet location ($\mathbf{x} \neq \mathbf{X}$). Let us consider the first case, where we want to calculate $\mathbf{u}(\mathbf{X})$ at time index n. We replace the velocity on the left-hand side of Equation (31) with a forward difference to obtain

$$\frac{\mathbf{X}^{n+1} - \mathbf{X}^{n}}{\Delta t} = \mathbf{u}_{\mathrm{bg}}(\mathbf{X}^{n}) + M(\mathbf{X}^{n}, \mathbf{X}^{n})\mathbf{X}^{n+1}, \tag{33}$$

where superscripts denote the time index. Note from Equation (33) that the background velocity and the regularized Stokeslets are computed with the current position of the fiber, $\mathbf{X}^n$, but the regularized Stokeslets are applied to forces generated by the new fiber position, $\mathbf{X}^{n+1}$. A benefit of using this time-stepping scheme is that the solution can be found by solving a linear system

$$\mathbf{X}^{n+1} = [I - \Delta t M(\mathbf{X}^{n}, \mathbf{X}^{n})]^{-1} \left(\mathbf{X}^{n} + \Delta t \mathbf{u}_{\mathrm{bg}}(\mathbf{X}^{n})\right). \tag{34}$$

Thus, Equation (34) is used to update the position of the fiber at each time step while maintaining a balance between avoiding prohibitively small time steps and solution of nonlinear systems.

We also have to consider updating the position of tracer particles that do not coincide with the regularized Stokeslet locations by discretizing $\mathbf{u}(\mathbf{x})$ in time. However, now that we know the updated fiber position, $\mathbf{X}^{n+1}$, we can explicitly solve Equation (31) for the updated fluid tracer position

$$\mathbf{x}^{n+1} = \mathbf{x}^{n} + \Delta t \left[\mathbf{u}_{\mathrm{bg}}(\mathbf{x}^{n}) + M(\mathbf{x}^{n}, \mathbf{X}^{n})\mathbf{X}^{n+1}\right]. \tag{35}$$

Using Equations (34) and (35), we can now update the position of the fluid particle at any location, regardless of whether it coincides with a regularized Stokeslet location.

4. NUMERICAL RESULTS

A goal of modeling approximately inextensible, semi-flexible fibers in cellular Stokes flow with regularized Stokeslets is to capture the qualitative behavior of a filament that is observed in the experiments of Wandersman *et al.* [38] and reported in the model of Young and Shelley [29]. Wandersman *et al.* observed that a fairly flexible fiber bends as it navigates through the stagnation points. However, when the bending rigidity of the fiber is increased, the fiber pivots at the stagnation points instead of bending. Some of the results in [29] show buckling behavior for a semi-flexible fiber as well.

To compare the regularized Stokeslets model to the results of Wandersman *et al.*, we use the following parameters that are used in their experiments. The fiber has length of $L_0 = 12$ mm and radius $r = 90$ μm. The Young's modulus, Y, is allowed to take on values ranging from 75 to 180 kPa. We will use both extremes of this range to model two fibers of different rigidity. The cellular background flow has a cell size of $W = 3$ cm, which makes the ratio of fiber length to cell width $\alpha = \frac{L}{W} = 0.4$ in this case. The viscosity of the fluid is $\mu = 40$ mPa s, and the maximum speed is $u_0 = 17$ mm/s, which creates a maximum extension rate near a stagnation point of $\dot{\gamma}$ =1.78 s^{-1}. By choosing $Y = 75$ kPa, the fiber is more semi-flexible than when $Y = 180$ kPa. The results shown in this section are produced with a dimensionless model. Incorporating the aforementioned physical parameters results in the following model parameters: effective viscosity $\eta' = \frac{\mu \dot{\gamma} L_0^4}{B}$, bending rigidity

DOI: 10.1002/cnm

$B = \frac{\pi r^4 Y^4}{4}$, tension coefficient $T_0 = \frac{\eta' \dot{\gamma}}{L_0^2}$, and bending coefficient $c_b = 1$. The fiber is discretized using $N = 100$ regularized Stokeslets with spreading parameter $\epsilon = 0.001$. The time step used is 0.001 in dimensionless time units (when time and distance are nondimensionalized using $\dot{\gamma} = 1.78$ s^{-1} and $L_0 = 12$ mm, respectively).

The results for both of the semi-flexible ($Y = 75$ kPa) and stiff ($Y = 180$ kPa) cases are shown in Figures 2 and 3, respectively. In these figures, the fiber begins in a vertical position slightly offset to the right of the stable manifold. The initial position of the bottom end of the fiber is $(3 \times 10^{-3}, 3 \times 10^{-6})$ cm when a stagnation point coincides with the origin, and the cell width is $W = 3$ cm. The physical parameters and initial conditions are identical for these two cases, with the exception of the Young's modulus. As time passes, the fiber travels down toward the stagnation point, hovers over it, buckles (Figure 2(c) for the semi-flexible fiber) or pivots (Figure 3(c) for the stiff fiber), and travels away from the stagnation point on the unstable manifold. This behavior is consistent with the experimental results shown in Figure 1 of [38].

For a slightly different choice of parameters, a semi-flexible fiber can produce the s-shaped buckle that is discussed in Young and Shelley [29]. This fiber has bending rigidity $B = 10^{-15}$ N m^2, dimensionless effective viscosity of $\eta' = 10^4$, tension coefficient $T_0 = 9.9 \times 10^7$, and bending coefficient $c_b = 99$. The fiber starts vertically, parallel to the stable manifold, with its lowest point at $(3 \times 10^{-7}, 0)$ cm. The fiber has length of $L_0 = 1$ cm and the cell width is $W = 3$ cm. In this case, the dimensionless time is scaled by $\dot{\gamma} = 1$ s^{-1}. The time step is $\Delta t = 0.001$ s, and we use $N = 100$ regularized Stokeslets with $\epsilon = 0.001$. The fiber in Figure 4 demonstrates the type of buckling behavior documented in Figure 1(a) of [29].

Although each panel in Figures 2–4 shows only one snapshot of the interaction of the fiber with a stagnation point, when viewed over a longer period, the fiber migrates from cell to cell. As it approaches a stagnation point, it chooses to bend/buckle/pivot, samples its local fluid velocity, and then chooses a direction to travel away from the original stagnation point. Figure 5 shows the center of mass of the fiber depicted in Figure 4 over a period of 400 s. This motion is qualitatively similar to that displayed in Figure 1(a) of [29].

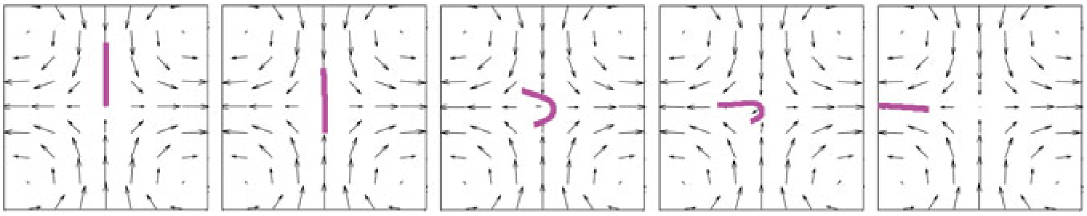

(a) $t = 0$ (b) $t = 2$ (c) $t = 4$ (d) $t = 6$ (e) $t = 8$

Figure 2. Snapshots of a semi-flexible fiber near a stagnation point obtained for $Y = 75$ kPa. The fiber approaches the stagnation point vertically, hovers, buckles, and exits to the left. The given time values are dimensionless (nondimensionalized by $\dot{\gamma} = 1.78$ s^{-1}).

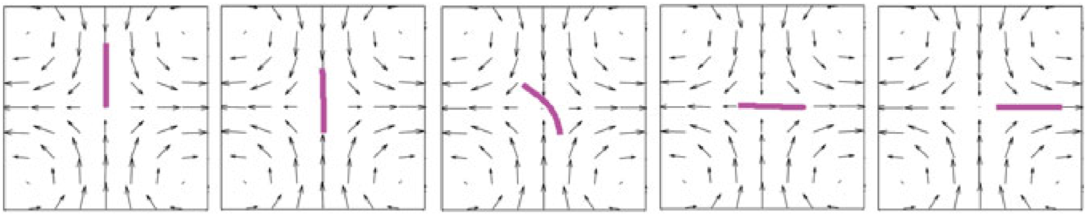

(a) $t = 0$ (b) $t = 2$ (c) $t = 4$ (d) $t = 6$ (e) $t = 8$

Figure 3. Snapshots of a stiff fiber near a stagnation point obtained for $Y = 180$ kPa. The fiber approaches the stagnation point vertically, hovers, pivots, and exits to the right. The given time values are dimensionless (nondimensionalized by $\dot{\gamma} = 1.78$ s^{-1}).

DOI: 10.1002/cnm

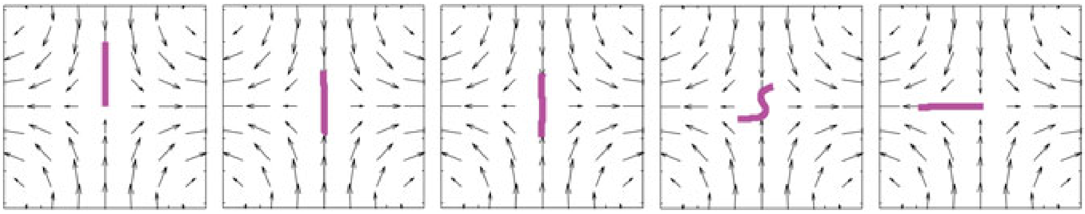

(a) $t = 0$ (b) $t = 2.5$ (c) $t = 5$ (d) $t = 7.5$ (e) $t = 10$

Figure 4. Snapshots of another semi-flexible fiber near a stagnation point. The fiber approaches the stagnation point vertically, hovers, buckles, and exits to the left. The given time values are dimensionless (nondimensionalized by $\dot{\gamma} = 1\ \mathrm{s}^{-1}$).

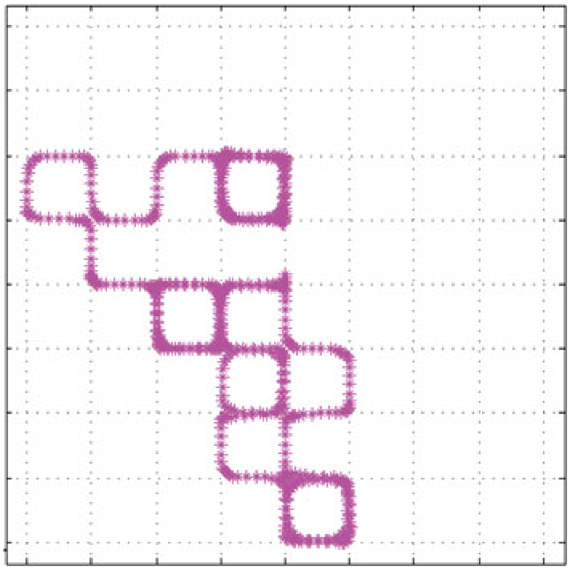

Figure 5. Trajectory of the center of mass of the fiber depicted in Figure 4 over a period of 400 s.

Beyond qualitative benchmarking with the experimental and modeling results in the literature, one advantage to using the method of regularized Stokeslets to model an immersed fiber is the ability to calculate the stress exerted by the fiber on the fluid with Equation (23). The dynamics of the elastic fiber around the stagnation point in the extensional flow is of specific interest.

In experiments of microfluidic extensional cross-flow with polymer molecules, it is observed that the polymers are strongly stretched near the stagnation point, and the fluid flow can exhibit nonlinear behavior such as bistability [27, 40–42]. At low Weissenberg numbers, the ratio of filament relaxation time to the characteristic fluid flow time scale, the flow remains steady but becomes asymmetrically deformed. At high Weissenberg numbers, the velocity field is unsteady and produces mixing. Numerical studies of this experiment have found instabilities for large Weissenberg numbers, even though the wide-band spectra in experiments have not been observed in numerical studies [43, 44].

Analytical studies of Stokesian non-Newtonian fluids show that the spatial structures of the stress field are very sensitive to the Weissenberg number [43]. At high Weissenberg numbers, the stress fields tend to develop nearly singular spatial variation, which is closely related to the aforementioned bistability. For the simulations shown in Figures 2 and 3, the estimated Weissenberg number is in the approximate range $1 < Wi < 6$, which is similar to those in microchannel experiments. Therefore, it would be interesting to examine the stress tensor in more details.

Figures 6 and 7 show the components of the stress tensor for the time snapshots denoted by time $t = 4$ in Figures 2(c) and 3(c), respectively. The divergence of stress is related to the forces exerted

DOI: 10.1002/cnm

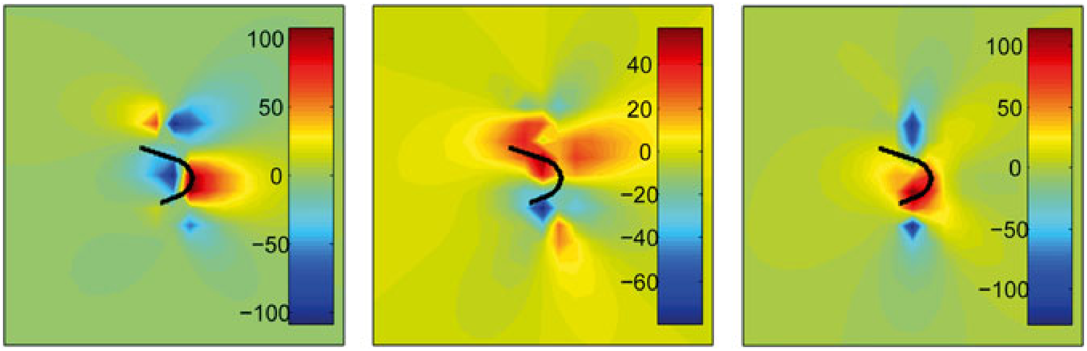

(a) σ_{11} (b) $\sigma_{12}=\sigma_{21}$ (c) σ_{22}

Figure 6. Stress tensor components for a semi-flexible fiber in the configuration shown in Figure 2(c).

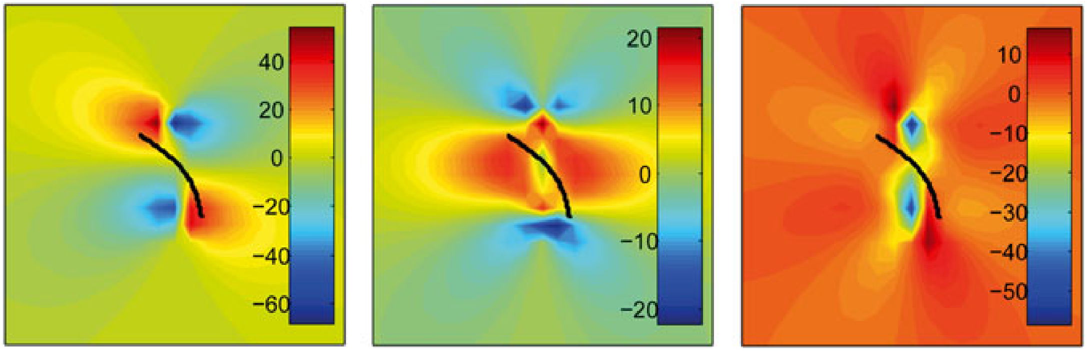

(a) σ_{11} (b) $\sigma_{12}=\sigma_{21}$ (c) σ_{22}

Figure 7. Stress tensor components for a stiff fiber in the configuration shown in Figure 3(c).

on the fluid from the elastic filament (e.g., see [27], [39]). One would expect the stress fields to be different for the semi-flexible and rigid cases as the fiber deformation is significantly different as it passes the stagnation point in the extensional flow, as shown in Figures 6 and 7. Notice that the spatial structure of the stress field differs in these two cases. Also, the extreme stress values are larger in all stress components for the semi-flexible case compared with the stiff case.

Figure 8 shows the temporal variation of the stress fields, with Figure 8(a, b) corresponding to the semi-flexible and stiff fiber motion, depicted in Figures 2 and 3, respectively. Given a fixed x position, the largest magnitude of stress component σ_{11} is plotted versus time. Because of the fact that the different fibers exit the stagnation points in different directions, different x values are sampled. For the semi-flexible fiber, the x values used are 0.5, 0.75, and 1 cm, where the origin coincides with the stagnation point and the cell width is $W=3$ cm. The x values used for the stiff case are -0.5, -0.75, and -1 cm. The curvature is also plotted as a function of time in Figure 8 for reference.

As the semi-flexible fiber buckles near the stagnation point for time $3<t<7$ in Figure 8, the stress field first increases in amplitude and then decays as the fiber moves away from the stagnation point. For the stiff fiber, rotation and slight filament deformation around the stagnation point lead to an increase in the stress field for time $4<t<7$. However, the increase in stress follows the increase in curvature that occurs for time $3<t<5$, unlike in the semi-flexible case where they coincide. In both cases, the stress is non-zero when the fiber travels to the stagnation point and hovers before deciding to buckle or pivot. The magnitude of the stress for time $0<t<3$ is larger in the semi-flexible case rather than the stiff case, but the opposite is true for $t>3$. It should be noted that whereas the x values sampled in these plots are symmetric about the y axis, the symmetry is not present in the stress plots in Figure 8 because of the position of the fiber relative to the fixed x values. Although the fiber does not cross the $x=-0.5$-cm line, it comes much closer to it while pivoting than the semi-flexible fiber does to $x=0.5$ cm while buckling, suggesting why the stress

DOI: 10.1002/cnm

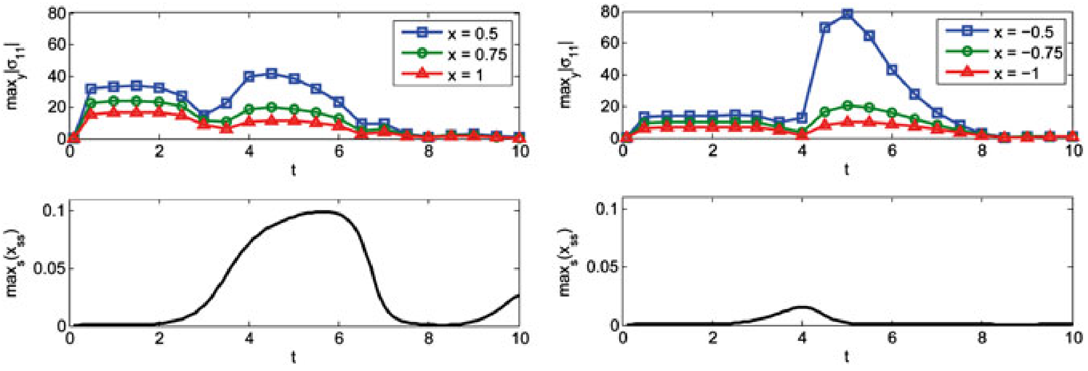

(a) Semi-flexible fiber.

(b) Stiff fiber.

Figure 8. The top plots show maximum of stress tensor component σ_{11} versus time for three fixed x locations. The semi-flexible fiber case is shown in (a) for $x = 0.5$, 0.75, and 1 cm. The stiff fiber case is shown in (b) for $x = -0.5$, -0.75, and -1 cm. The bottom row of plots show the maximum curvature of the fiber versus time.

is higher in the stiff case than in the semi-flexible case, despite the curvature. Additionally, as seen in Figures 6 and 7, the spatial structure of the stress is different for both the semi-flexible and stiff cases, providing an explanation for why the plots of stress versus time are not identical.

To view the time evolution of stress in a different way, Figure 9 displays the stress component σ_{11} at $x = 0.5$ cm as a function of y for various times. The spatial structure of the stress fields when the fiber is bent (e.g., when $t = 4$ in Figure 9) exhibits similar features in the analysis of Olroyd-B extensional flow in Figure 5 of [43].

The pressure for both the semi-flexible and stiff fibers is given in Figure 10 to give a complete description of the fluid. Notice, as with the stress, that the extreme values of the pressure in the semi-flexible fiber case are larger in magnitude than those in the stiff case.

5. MULTIPLE FIBERS

Modeling the hydrodynamic interactions between multiple filaments has a variety of applications from polymer suspensions to non-Newtonian fluids. The method of regularized Stokeslets can be used to model multiple immersed bodies in addition to the earlier single fiber studies. The formulation given in Equation (30) only needs to be modified slightly to model multiple fibers. Namely, the elastic and bending forces need to be formulated in such a way that the positions of the regularized Stokeslets constituting a particular fiber only affect the elastic and bending forces calculated on that same fiber. In the notation of Equation (30), let $\mathbf{X}$ contain all regularized Stokeslets but arrange the

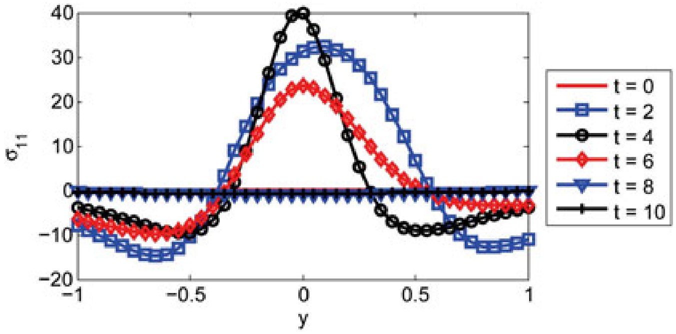

Figure 9. Stress component σ_{11} at fixed $x = 0.5$ cm as a function of vertical position y for the semi-flexible fiber shown in Figure 2. Each curve represents a different dimensionless time value.

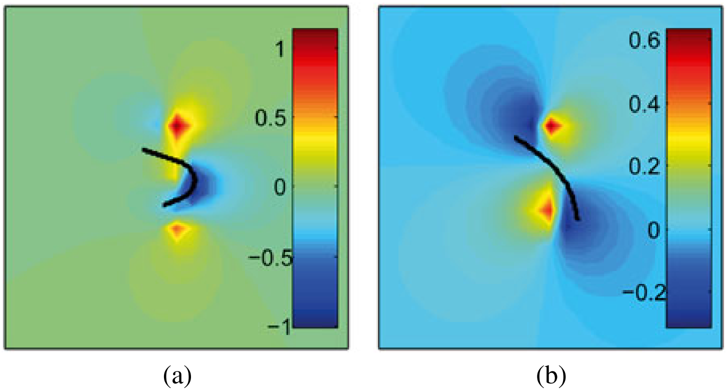

Figure 10. Pressure for semi-flexible and stiff fibers in the configurations shown in (a) Figure 2(c) and (b) Figure 3(c).

elements of **X** so that the points composing each fiber are grouped together. Correspondingly, A_e and A_b become block diagonal matrices, where each block contains the discretization discussed in Section 3.1.

Consider modeling two fibers immersed in cellular Stokes flow, one of which has the same initial parameters to the semi-flexible fiber shown in Figure 2. The second fiber has identical parameters to the first with the exception of initial position. With the stagnation point labeled as the origin and a cell width of $W = 3$ cm, the second fiber begins in a horizontal position with its left-most point located at $(0.3, 3 \times 10^{-6})$ cm. The top row in Figure 11 shows the flow resulting from the immersed fiber shown in Figure 2 (although at different time increments), whereas the bottom row of Figure 11 shows the multiple fiber case discussed above. Notice that the presence of the second fiber quickly affects the buckling structure of the first fiber compared with its model in isolation.

In [45], slender-body formulation was used to simulate the motion of two immersed fibers. That approach prevents the fibers from intersecting by imposing artificial forces on the fibers. However, there are no such forces in the model presented in this paper. A more detailed exploration of modeling multiple immersed fibers with regularized Stokeslets is a direction of future work.

6. CONCLUSIONS

In this study, we implement the method of regularized Stokeslets to model a semi-flexible, approximately inextensible fiber immersed in two-dimensional cellular Stokes flow. The method of regularized Stokeslets provides a way to calculate the fluid velocity anywhere in the fluid domain

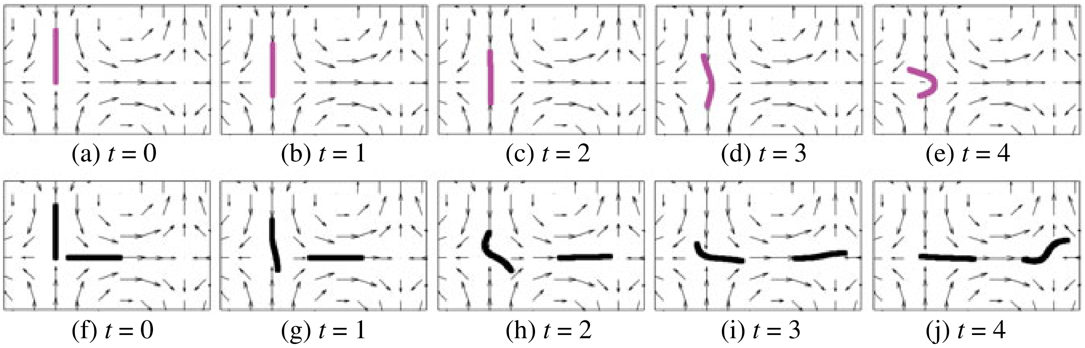

Figure 11. The immersed fiber in Figure 2 is shown at different time increments here in (a)–(e). A second identical fiber (with the exception of initial position) is added to the flow in (f)–(j). Notice that the presence of the second fiber quickly affects the buckling behavior of the original fiber.

due to regularized forces exerted on the fluid. The fiber modeled with the method of regularized Stokeslets shows qualitative agreement with the experimental observations of Wandersman *et al.* [38], changing its behavior near stagnation points as the physical parameters change.

Young and Shelley have modeled this scenario by using slender-body theory, but using the method of regularized Stokeslets to model this system can provide additional information and flexibility. In particular, the stress induced by the fiber can be calculated with the method of regularized Stokeslets. The regularized expressions for velocity, stress, and pressure in two dimensions are derived following [31]. The regularized Stokeslet modeling results are qualitatively in agreement with those of Young and Shelley [29]. In calculating the stress and pressure for both semi-flexible and stiff fibers, the results presented here show interesting connections between fiber curvature and spatial stress distribution.

A possible direction of future inquiry is in comparing the effects of treating the fiber's inextensibility condition as a chain of stiff Hookean springs versus a line tension formulation. In addition, continued modeling of multiple immersed fibers with regularized Stokeslets is a direction for future work. Careful comparisons with the slender-body results in [45] and modeling more immersed fibers are probable directions for future investigation. The possible future directions of this work provide an opportunity to explore other immersed structures that interest both the biological and fluid dynamics communities.

ACKNOWLEDGEMENTS

Layton acknowledges support from NSF grant DMS-0701412. Young acknowledges support from NSF grants CBET-0853673 and DMS-0708977.

REFERENCES

1. Cartwright JHE, Piro N, Piro O, Tuval I. Embryonic nodal flow and the dynamics of nodal vesicular parcels. *Journal of Royal Society Interface* 2007; **4**(12):49–55.
2. Cartwright JHE, Piro O, Tuval I, Kadanoff L. Fluid-dynamical basis of the embryonic development of left-right asymmetry in vertebrates. *Proceedings of the National Academy of Science of the United States of America* 2004; **101**(19):7234–7239.
3. Hirokawa N, Tanaka Y, Okada Y, Takeda S. Nodal flow and the generation of left–right asymmetry. *Cell* April 7 2006; **125**:33–24.
4. Nonaka S, Tanaka Y, Okada Y, Takeda S, Kido M, Hirokawa N. Randomization of left–right asymmetry due to loss of nodal cilia generating leftward flow of extraembryonic fluid in mice lacking KIF3B motor protein. *Cell* 1998; **95**:829–837.
5. Okada Y, Takeda S, Tanaka Y, Belmonte J-CI, Hirokawa N. Mechanism of nodal flow: a conserved symmetry breaking event in left–right axis determination. *Cell* 2005; **121**:633–644.
6. Berg HC, Anderson RA. Bacteria swim by rotating their flagellar filaments. *Nature* 1973; **245**:380–382.
7. Meister M, Berg HC. Rapid rotation of flagellar bundles in swimming bacteria. *Nature* 1987; **325**:637–640.
8. Silverman M, Simon M. Flagellar rotation and the mechanism of bacterial motility. *Nature* 1974; **249**:73–74.
9. Kulic IM, Brown AEX, Kim H, Kural C, Blehm B, Selvin PR, Nelson PC, Gelfand VI. The role of microtubule movement in bidirectional organelle transport. *Proceedings of the National Academy of Science of the United States of America* 2008; **105**(29):10011–10016.
10. Welte MA. Bidirectional transport along microtubules. *Current Biology* 2004; **14**(13):R525–R537.
11. Bourdieu L, Duke T, Elowitz MB, Winkelmann D, Leibler S, Libchaber A. Spiral defects in motility assays: a measure of motor protein force. *Physical Review Letters* 1995; **75**:176–179.
12. Bourdieu L, Magnasco MO, Winkelmann DA, Libchaber A. Actin filaments on myosin beds: the velocity distribution. *Physical Review E* 1995; **52**:6573–6579.
13. Hamelink W, Zegers JG, Treijtel BW, Blange T. Path reconstruction as a tool for actin filament speed determination the in vitro motility assay. *Analytical Biochemistry* 1999; **273**:12–19.
14. Clemmens J, Hess H, Doot R, Matzke CM, Bachand GD, Vogel V. Motor-protein "roundabouts": microtubules moving on kinesin-coated tracks through engineered networks. *Lab on a Chip* 2004; **4**:83–86.
15. Hess H, Clemmens J, Qin D, Howard J, Vogel V. Light-controlled molecular shuttles made from motor proteins carrying cargo on engineered surfaces. *Nano Letters* 2001; **1**:235–239.
16. Hess H, Matzke CM, Doot RK, Clemmens J, Bachand GD, Bunker BC, Voger V. Molecular shuttles operating undercover: a new photolithographic approach for the fabrication of structured surfaces supporting directed motility. *Nano Letters* 2003; **3**:1651–1655.
17. Jia L, Moorjani SG, Jackson TN, Hancock WO. Microscale transport and sorting by kinesin molecular motors. *Biomedical Microdevices* 2004; **6**:67–74.

DOI: 10.1002/cnm

18. Limberis L, Stewart RJ. Toward kinesin-powered microdevices. *Nanotechnology* 2000; **11**:47–51.
19. van den Heuvel MGL, Dekker C. Motor proteins at work for nanotechnology. *Science* 2007; **317**:333.
20. Hess H, Clemmens J, Brunner C, Doot R, Luna S, Ernst K-H, Vogel V. Molecular self-assembly of “nanowires” and “nanospools” using active transport. *Nano Letters* 2005; **5**:629–633.
21. van den Heuvel MGL, de Graaff MP, Dekker C. Molecular sorting by electrical steering of microtubules in kinesin-coated channels. *Science* 2006; **312**:910–914.
22. Yokokawa B, Takeuchi S, Kon T, Nishiura M, Sutoh K, Fujita H. Unidirectional transport of kinesin-coated beads on microtubules oriented in a microfluidic device. *Nano Letters* 2004; **4**:2265–2270.
23. Kim T, Kao M-T, Hasselbrink EF, Meyhöfer E. Nanomechanical model of microtubule translocation in the presence of electric fields. *Biophysical Journal* 2008; **94**:3880–3892.
24. Kim T, Kao M-T, Meyhofer E, Hasselbrink EF. Biomolecular motor-driven microtubule translocation in the presence of shear flow: analysis of redirection behaviours. *Nanotechnology* 2007; **18**:025–101.
25. Nitta T, Tanahashi A, Hirano M, Hess H. Simulating molecular shuttle movements: towards computer-aided design of nanoscale transport systems. *Lab on a Chip* 2006; **6**:881–885.
26. Nitta T, Tanahashi A, Obara Y, Hirano M, Razumova M, Regnier M, Hess H. Comparing guiding track requirements for myosin- and kinesin-powered molecular shuttles. *Nano Letters* 2008; **8**:2305–2309.
27. Schroeder CM, Babcock HP, Shaqfeh ESG, Chu S. Observation of polymer conformation hysteresis in extensional flow. *Science* 2003; **301**:1515–1519.
28. Tornberg A-K, Shelley MJ. Simulating the dynamics and interactions of elastic filaments in Stokes flows. *Journal of Computational Physics* 2004; **196**:8–40.
29. Young Y-N, Shelley MJ. A stretch–coil transition and transport of fibers in cellular flows. *Physical Review Letters* 2007; **99**:058–303.
30. Lim S, Ferent A, Wang XS, Peskin CS. Dynamics of a closed rod with twist and bend in fluid. *Society for Industrial and Applied Mathematics Journal on Scientific Computing* 2008; **31**:273–302.
31. Cortez R. The method of regularized Stokeslets. *Society for Industrial and Applied Mathematics Journal on Scientific Computing* 2001; **23**(4):1204–1225.
32. Cortez R, Fauci L, Medovikov A. The method of regularized Stokeslets in three dimensions: analysis, validation, and application to helical swimming. *Physics of Fluids* 2005; **17**(3):031504.1–031504.14.
33. Ainley J, Durkin S, Embid R, Boindala P, Cortez R. The method of images for regularized Stokeslets. *Journal of Computational Physics* 2008; **227**:4600–4616.
34. Bouzarth EL. Regularized singularities and spectral deferred correction methods: a mathematical study of numerically modeling stokes fluid flow. *PhD Thesis*, The University of North Carolina at Chapel Hill 2008. URL http://dc.lib.unc.edu/u?/etd,1917.
35. Bouzarth EL, Minion ML. A multirate integrator for regularized Stokeslets. *Journal of Computational Physics* 2010; **229**:4208–4224.
36. Cummins B, Gedeon T, Klapper I, Cortez R. Interaction between arthropod filiform hairs in a fluid environment. *Journal of Theoretical Biology* 2007; **247**:266–280.
37. Flores H, Lobaton E, Méndez-Diez S, Tlupova S, Cortez R. A study of bacterial flagellar bundling. *Bulletin of Mathematical Biology* 2005; **67**:137–168.
38. Wandersman E, Quennouz N, Fermigier M, Lindner A, Roure ODu. Buckled in translation. *Soft Matter* 2010; doi 10.1039/C0SM00132E. URL http://dx.doi.org/10.1039/C0SM00132E.
39. Pozrikidis C. *Boundary Integral and Singularity Methods for Linearized Viscous Flow*. Cambridge University Press, 1992.
40. Arratia PE, Thomas CC, Diorio J, Gollub JP. Elastic instabilities of polymer solutions in cross-channel flow. *Physical Review Letters* 2006; **96**:144–502.
41. de Gennes PG. Coil–stretch transition of dilute flexible polymers under ultrahigh velocity gradients. *Journal of Chemical Physics* 1974; **60**:5030–5042.
42. Smith DE, Babcock HP, Chu S. Single polymer dynamics in steady shear flow. *Science* 1999; **283**:1724.
43. Thomases B, Shelley M. Emergence of singular structures in Oldroyd-B fluids. *Physics of Fluids* 2007; **19**:103–103.
44. Thomases B, Shelley M. Transition to mixing and oscillations in a Stokesian viscoelastic flow. *Physical Review Letters* 2009; **103**:094–501.
45. Young Y-N. Hydrodynamic interactions between two semiflexible inextensible filaments in stokes flow. *Physical Review E* 2009.

DOI: 10.1002/cnm